



This is the accepted manuscript made available via CHORUS. The article has been published as:

Tunable magnetic anisotropy in multiferroic oxides

Xue-Zeng Lu and James M. Rondinelli

Phys. Rev. B **103**, 184417 — Published 17 May 2021

DOI: 10.1103/PhysRevB.103.184417

Tunable Magnetic Anisotropy in Multiferroic Oxides

Xue-Zeng Lu and James M. Rondinelli

Department of Materials Science and Engineering, Northwestern University, Evanston, Illinois

60208, USA

E-mail: jrondinelli@northwestern.edu

Abstract

Room-temperature electric-field control of magnetism is actively sought to realize electric-field

assisted changes in perpendicular magnetic anisotropy (PMA), which is important to magnetic

random access memories (MRAMs) and future spin-orbit based logic technologies. Traditional

routes to achieve such control rely on heterostructures of ferromagnets and/or ferroelectrics,

exploiting interfacial effects, including strain generated by the substrate, or electric-field induced

changes in the interfacial electronic structures. Here we present design rules based on d-orbital

splitting in an octahedral field and crystallographic symmetries for electric-field control of PMA

utilizing hybrid improper ferroelectricity by scaffolding simple perovskite oxides into ultrashort

period superlattices, (ABO₃)₁/(A'BO₃)₁, and in multiferroic AA'BB'O₆ double perovskites. We

validate the strategy using first-principles calculations and a single-ion anisotropic model. We find

a change in the magnetic anisotropy from the in-plane to out-of-plane direction in

(BiFeO₃)₁/(LaFeO₃)₁ and a 50% decrease of the magnetization along the *out-of-plane* direction in

LaYNiMnO₆, when a polar-to-nonpolar phase transition occurs with strain. The origin of the PMA

control is due to the structural-tunable competitions among the t_{2g} and e_g orbital interactions on

the magnetic ions arising from relativistic spin-orbital interactions that are susceptible to changes

in the oxygen octahedral tilts across the field-tunable transition. Our results allow us to search

rapidly for other promising multiferroics materials with voltage-controlled magnetic anisotropy

for applications in low-energy information storage and logic devices.

1. Introduction

Electric-field controllable magnetism (EFCM) offers a route towards low-energy information

storage and new forms of logic devices [1,2]. Several strategies were reported in ferromagnetic films or semiconductors [3-6], magnetoelectric multiferroics [7-9], heterostructures or superlattices consisting of ferromagnets and/or ferroelectrics [10-17], multidomain and domain wall structures [18-26], perovskites thin films [27-29], and hybrid improper ferroelectrics [30-33]. The aspirational goal of these materials platforms is to realize tunable perpendicular magnetic anisotropy (PMA) [34,35], with most realizations of electric-field assisted changes in PMA occurring in ferromagnetic films on semiconductors [3-6] or in ferromagnets and/or ferroelectrics heterostructures [12-15,34]. Materials and mechanisms to realize electric-field controllable PMA in multiferroics with large ferroelectricity (e.g., > 1 C/m²) and strong ferromagnetism (e.g., > 1 μ_B per transition-metal ion) at room temperature, however, remains a challenge [35], despite experimentally demonstrated electric-field control of in-plane magnetic anisotropy in BiFeO₃ [19,20,22] and predicted control in LiNbO₃-type Zn₂FeO₅O₆ [36] and double perovskite LaSrMnOsO₆ [37]. From a processing perspective, it is desirable to realize PMA control from single phase (multiferroic) components rather than requiring complex multi-component heterostructures.

In 2011, Benedek and Fennie proposed hybrid improper ferroelectricity (HIF) is active in Ruddlesden–Popper Ca₃B₂O₇ (B=Mn,Ti) materials [30], which was experimentally demonstrated later [38-41]. In these compounds, the polar mode $(Q_{\Gamma_5^-})$, oxygen octahedral rotation (OOR) $(Q_{X_2^+})$, and oxygen octahedral tilt (OOT) $(Q_{X_3^-})$ modes couple through a trilinear interaction, $Q_{\Gamma_5^-}Q_{X_2^+}Q_{X_3^-}$, to stabilize the polar ground state structure with $Cmc2_1$ symmetry. The functional electric

polarization P is proportional to $Q_{X_2^+}Q_{X_3^-}$ owing to the HIF mechanism. Moreover, the direction of weak ferromagnetism (wFM), which is due to the antisymmetric Dzyaloshinskii-Moriya (DM) exchange interaction, is controlled by the tilt $Q_{X_3^-}$ mode (OOT) that occurs about the short crystallographic axes in the magnetic members of this family. Here, the direction of the wFM can be switched by an *in-plane* electric field through coupling to the polarization, which in turn reverses the $Q_{X_3^-}$ mode. Later, the HIF mechanism was extended to 1/1 period A-site cation ordered perovskite superlattices [33], which led to the theoretical prediction of ultrashort period BiFeO₃/LaFeO₃ superlattices exhibiting room-temperature EFCM [42]. To the best of our knowledge, reported EFCM mechanisms rely on the aforementioned DM-induced wFM controlled by the OOT mode [30]. The tunable wFM induced by the DM interactions is also key to other promising candidates for the EFCM in multiferroics at room temperature [43,44]. Remarkably, there are no assessments concerning the viability of electric-field tunable magnetic anisotropy in HIF materials despite the potential of HIF to serve as a novel mechanism from which to design multiferroics exhibiting simultaneously large ferroelectricity, strong ferromagnetism, and strong magnetoelectricity.

Here, we propose design rules to tune the magnetic anisotropy, which may be used to explore electric field control of perpendicular magnetic anisotropy, utilizing a combination of density functional theory (DFT) calculations and single-ion anisotropic models, in (ABO₃)₁/(A'BO₃)₁ superlattices and AA'BB'O₆ double perovskites exhibiting HIF. We first show a change of the magnetic anisotropy from an *in-plane* to *out-of-plane* direction in experimentally synthesizable

BiFeO₃/LaFeO₃ superlattices across an electric-field driven polar-to-nonpolar (P-to-NP) phase transition. Next, we find a 50% decrease of the magnetization along the out-of-plane direction in double perovskite LaYNiMnO₆ across an analogous P-to-NP phase transition. The tunable magnetic anisotropy is due to the changes in the oxide ligand fields about the magnetic ions induced by changes in the character of the oxygen octahedral tilts across the transition. This tiltanisotropy sensitivity arises from the spin-orbital interactions (SOI) among the t_{2g} and e_g orbitals on the magnetic ions, which can either produce easy-plane or easy-axis anisotropies, because SOI are controlled by the oxygen octahedral tilt symmetry. From this understanding, we formulate two design principles for ferroelectric control of the magnetic anisotropy: 1) orbital splitting criterion: selecting d^n magnetic ions with the highest-occupied or lowest-unoccupied orbitals of xy symmetry to be nearly degenerate with at least one of the other two t_{2g} orbitals (such as, Mn^{4+} with d^3 and Fe³⁺ d^5 configurations); and 2) polymorphism criterion: a ferroelectric phase with a low-energy metastable state exhibiting either an abrupt change in magnitude or distinct change in pattern of the oxygen octahedral tilts (such as in the P-to-NP transition). Our study calls for careful examination on the magnetic anisotropy changes that occur along with structural phase transitions in other multiferroics materials.

2. Tunable magnetic anisotropy

2.1 Polar-to-nonpolar phase transitions in 1:1 BiFeO₃/LaFeO₃ superlattice

We showed previously that the P-to-NP transition is a general feature in $(ABO_3)_1/(A'BO_3)_1$ superlattices and $AA'BB'O_6$ double perovskites exhibiting HIF [45], because the hidden nonpolar

phase originates from the competition between the anharmonic (trilinear) octahedral-derived mode interactions that stabilize HIF in the polar phase and hybrid improper antiferroelectricity in the nonpolar phase. Figure 1a shows a similar P-to-NP (Pmc2₁-to-P2₁/m symmetry) transition occurs at $\approx 0.5\%$ strain in the BiFeO₃/LaFeO₃ superlattice, and that tensile strain favors the polar *Pmc*2₁ phase whereas compressive strain favors the nonpolar $P2_1/m$ phase. This ferrate strain-phase diagram is consistent with other (ABO₃)₁/(A'BO₃)₁ superlattices [45]. At the Pmc2₁-to-P2₁/m transition there is a sudden decrease in electric polarization from 4µC/cm² to zero at 0.5% strain. Because of the trilinear couplings among P, OOT, and OOR modes in $Pmc2_1$, the transition also changes the character of the OOT and OOR modes. The OOT mode along [110] transforms into two unique and independent OOT along [100] and along [010], while the OOR become out-ofphase in the $P2_1/m$ phase (see inset of Figure 1a and details below). The corresponding changes in the magnitudes of the OOT and OOR modes are very small. Although previous reports showed the polar *Pmc*2₁ phase remains stable at -1% strain (corresponding to -1.1% in our definition) [42], this quantitative value for the critical strain may be due to the different exchange-correlation functional used. Ref. [42] uses the local spin density approximation with the plus Hubbard Ucorrection (LSDA+U) whereas we use the revised Perdew-Becke-Erzenhof functional for solids with the plus U method (PBEsol+U) following Ref. [44] (see, also, references [45-48] therein). The existence of the nonpolar $P2_1/m$ phase under strain is also supported by our Landau model and genetic algorithm (GA) structural search method [49,50].

2.2 Model analysis of the tunable magnetic anisotropy across the P-to-NP transition

Next we perform DFT+U+SOC (spin-orbital coupling) calculations and find that the *in-plane* magnetic anisotropy in the $Pmc2_1$ phase of the G-type antiferromagnetic (AFM) BiFeO₃/LaFeO₃ superlattice is along the $[1\bar{1}0]$ direction, which is perpendicular to the [110] electric polarization direction. This result is consistent with that in Ref. [42]. Interestingly, our calculations for the $P2_1/m$ phase indicate that the magnetic anisotropy changes to be along the [011] direction (Figure 1b). Thus, we expect that an *in-plane* electric field (E) may control the magnetic anisotropy across a $Pmc2_1$ -to- $P2_1/m$ (P-to-NP) transition through its coupling to the polarization (P) through the term $\propto P \cdot E$ in the free energy describing the compound.

To further elucidate the origins of the different magnetic anisotropies in the two phases, we next employ a phenomenological model with the spin Hamiltonian expressed as [51,52]:

$$\widehat{H}_{spin} = \sum_{i < j} J_{ij} \vec{\boldsymbol{S}}_i \cdot \vec{\boldsymbol{S}}_j + \sum_{i < j} \vec{\boldsymbol{D}}_{ij} \cdot (\vec{\boldsymbol{S}}_i \times \vec{\boldsymbol{S}}_j) + \sum_{i,\alpha\beta} A_{i,\alpha\beta} \vec{S}_{i\alpha} \vec{S}_{i\beta}$$
(1)

where J_{ij} and \vec{D}_{ij} are the symmetric spin-exchange and antisymmetric DM-exchange interaction parameters, respectively, between magnetic ions i with spin \vec{S}_i and j with \vec{S}_j . $A_{i,\alpha\beta}$ is the single-ion anisotropy parameter of ion i ($\alpha, \beta = x, y, z$). Although the DM-exchange interaction induces spin canting and may affect the magnetic anisotropy direction [36], SIA usually governs the principal spin direction. In addition, the spin canting angle is usually very small; for example, 0.7° in BiFeO₃/LaFeO₃ with a calculated wFM of ≈ 0.05 μ_B /Fe and a remnant moment of 4 μ_B /Fe [42]. Therefore, we focus on changes in the SIA term across the P-to-NP transition on the magnetic anisotropy, which we express as:

$$\widehat{H}_{SIA} = A_{i,xx}S_x^2 + A_{i,yy}S_y^2 + A_{i,zz}S_z^2 + 2A_{i,xy}S_xS_y + 2A_{i,xz}S_xS_z + 2A_{i,yz}S_yS_z = A_{i,xx}|\overrightarrow{S}|^2 + (A_{i,yy} - A_{i,xx})S_y^2 + (A_{i,zz} - A_{i,xx})S_z^2 + 2A_{i,xy}S_xS_y + 2A_{i,xz}S_xS_z + 2A_{i,yz}S_yS_z.$$
(2)

The effects of the DM-exchange interaction on the magnetic anisotropy can be found in Supplemental Material [53] (see, also, references [54, 55] therein).

We then compute the effective parameters $A_{i,yy} - A_{i,xx}$, $A_{i,zz} - A_{i,xx}$, $A_{i,xy}$, $A_{i,xz}$ and $A_{i,yz}$ using a four-states mapping method with our DFT+U+SOC calculations with $|\vec{S}| = 1$ for each phase at 0% strain. Next, we minimize \widehat{H}_{SIA} to obtain the SIA direction \vec{S} = $(\sin\theta\cos\varphi, \sin\theta\sin\varphi, \cos\theta)$ given by the polar (θ) and azimuthal (φ) angles as described in Ref. [53] (see, also, reference [56] therein). We find that the SIA on the single symmetry-unique iron site in the $Pmc2_1$ phase is close to the *in-plane* $[1\bar{1}0]$ direction $(\vec{S} = 0.62, -0.70, -0.36)$. In contrast, there are two symmetry-inequivalent Fe sites in the nonpolar $P2_1/m$ phase with the SIA very close to the [010] and [001] directions (Figure S2 and S3 in [53]), respectively, \vec{S}_1 = (-0.09, 0.94, 0.34) and $\vec{S}_2 = (-0.19, -0.30, -0.94)$. For each phase, we next minimize the sum of \widehat{H}_{SIA} over all iron sites in the unit cell to obtain the magnetic anisotropy and confirm the longrange spin order is G-type with our model, which agrees with our direct DFT+U+SOC calculations (Figure 1b). Therefore, we conclude here that the change in magnetic anisotropy across the P-to-NP transition originates from the dramatically different SIA on the iron sites, which the oxygen sublattice geometry imparts, i.e., the rotations, tilts, and other secondary distortions.

2.3 Effects of the phonon modes on the magnetic anisotropy

Displacive atomic distortions are known to affect SIA in magnetic materials [57,58]. Therefore, we next decompose the atomic displacements that produce the $Pmc2_1$ and $P2_1/m$ structures from the ideal P4/mmm high-symmetry structure into symmetry-adapted normal modes (Figure 2) to assess each modes contribution to the SIA. In the polar $Pmc2_1$ phase, there are three important modes: an in-plane ferroelectric (FE) mode along [110] transforming as the irreducible representation (irrep) Γ_5^- , an oxygen octahedral rotation (OOR) mode about [001] (M_2^+) , and an oxygen octahedral tilt (OOT) about [110] (M_5^-) . For the nonpolar $P2_1/m$ structure there are two inplane antiferroelectric (AFE) modes along [100] (Γ_5^+) and (N_3^-) , two AFE modes along [001] (N_3^-) and (N_3^-) and OOR about [001] (N_4^-) , and two OOTs about [100] and [010] (N_5^-) and (N_5^-) are the production of the magnetic anisotropy upon the phase transition.

By computing the SIA in a hypothetical structure, obtained from adding each mode with an amplitude given by the equilibrium phases at 0% strain into the P4/mmm structure, we obtain that modes contribution to the SIA (Figure 3). For the polar $Pmc2_1$ structure, both the Γ_5^- FE and M_2^+ OOR modes favor SIA close to the film normal direction, whereas the M_5^- OOT mode favors SIA close to the in-plane [1 $\bar{1}$ 0] direction. Thus, the OOT mode dominates among the SIA contributions to give the overall in-plane [1 $\bar{1}$ 0] magnetic anisotropy in the polar phase (Figure 1b). For the nonpolar $P2_1/m$ phase, we find the mode-dependent SIA is more complex, because there are more distortions and more sites to consider: the Γ_5^+ AFE mode favors SIA close to the [100] direction, the M_3^- AFE mode favors SIA in the (001) plane and is close to the [010] direction, the M_4^- OOR

mode favors out-of-plane SIA, the M_5^- OOT mode favors in-plane [010] SIA, the X_1^+ OOT mode favors in-plane [100] SIA, the X_2^- AFE mode favors SIA in the (010) plane and close to the [100] direction, and the X_3^- AFE mode favors SIA close to the [100] direction. We find that the values for the SIA parameters given by the Γ_5^+ and M_3^- AFE modes are small compared with other modes active in the $P2_1/m$ phase, suggesting that their effects on the SIA can be neglected (Figure 3a). Furthermore, the OOR (M_4^-) and OOT (M_5^-) and X_1^+) modes also lead to *in-plane* SIA, but close to the [110] direction, which indicates that the OOT modes also dominate the contributions from the OOR mode in the $P2_1/m$ phase—similar to our finding in the polar $Pmc2_1$ structure. The final magnetic anisotropy in the $P2_1/m$ phase must include contributions from the X_2^- and X_3^- AFE modes (Figure 3a). Because the OOR and OOT modes in both phases are primary modes stabilizing the nonpolar $P2_1/m$ symmetry [49], this mode- and site-resolved SIA assessment allows us to conclude that the decoupling of the OOT modes across the polar-tononpolar transition $(M_5^- \to M_5^- + X_1^+)$ sufficiently alters the Fe³⁺ coordination environments (inset of Figure 1a) so as to trigger a net change in the SIA direction from one phase to another.

2.4 Origin of the tunable magnetic anisotropy across the polar-to-nonpolar transition

The physical origin of SIA can be ascribed to SOC effects (i.e., $\lambda \hat{L} \cdot \hat{S}$) in perturbation theory [52,59], where $\lambda > 0$ if the orbital filling from unpaired electrons is less than half full for that manifold and $\lambda < 0$ otherwise. The $\lambda \hat{L} \cdot \hat{S}$ term can be further expanded as:

$$\lambda \hat{\boldsymbol{L}} \cdot \hat{\boldsymbol{S}} = \lambda \hat{S}_{z'} \left(\hat{L}_z \text{cos}\theta + \frac{1}{2} \hat{L}_+ e^{-i\varphi} \text{sin}\theta + \frac{1}{2} \hat{L}_- e^{i\varphi} \text{sin}\theta \right) + \frac{\lambda}{2} \hat{S}_{+'} (-\hat{L}_z \text{sin}\theta - \hat{L}_+ e^{-i\varphi} \text{sin}^2 \frac{\theta}{2} + \hat{L}_z \hat{S}_{+'} \hat{S}$$

$$\hat{L}_{-}e^{i\varphi}\cos^{2}\frac{\theta}{2}) + \frac{\lambda}{2}\hat{S}_{-'}\left(-\hat{L}_{z}\sin\theta + \hat{L}_{+}e^{-i\varphi}\cos^{2}\frac{\theta}{2} - \hat{L}_{-}e^{i\varphi}\sin^{2}\frac{\theta}{2}\right),\tag{3}$$

where the orbital angular momentum operator \hat{L} and spin angular momentum operator \hat{S} are in (x, y, z) and (x', y', z') Cartesian coordinates, respectively. θ and φ are the polar and azimuthal angles, respectively, of the spin direction (i.e., z' direction) with respect to the (x, y, z) coordinates. $\hat{L}_+ = \hat{L}_x + i\hat{L}_y$ and $\hat{L}_- = \hat{L}_x - i\hat{L}_y$ are ladder operators, and \hat{S}_+ and \hat{S}_- are specified in the same manner as \hat{L}_+ and \hat{L}_- , respectively. As shown from the electronic density of states (DOS) in Figure 4a, (additional details can be found in Ref. [53]), the Fe³⁺ d^5 orbital configurations in the two phases are similar and the energetic ordering and filling of the orbitals is approximately described as $(|xy\uparrow\rangle, |xz\uparrow\rangle, |yz\uparrow\rangle)^1 < (|x^2-y^2\uparrow\rangle, |z^2\uparrow\rangle)^1 < (|xy\downarrow\rangle, |xz\downarrow\rangle, |yz\downarrow\rangle)^0 < (|x^2-y^2\downarrow\rangle, |z^2\downarrow\rangle)^0$, where \uparrow and \downarrow represent spin-up and spin-down states, respectively. It should be noted that none of the orbitals are energetically degenerate owing to the reduced C_{2y} and C_{2h} Fe-site symmetries respectively, in the $Pmc2_1$ and $P2_1/m$ structures.

We focus on the SOC interactions between the $(|\mathbf{x}^2-\mathbf{y}^2\uparrow\rangle,|\mathbf{z}^2\uparrow\rangle)^1$ and $(|\mathbf{xy}\downarrow\rangle,|\mathbf{xz}\downarrow\rangle,|\mathbf{yz}\downarrow\rangle)^0$ states that occur due to the spin-non-conserving terms: $\widehat{H}'_{SO} = \frac{\lambda}{2}\widehat{S}_{+'}(-\widehat{L}_z\sin\theta - \widehat{L}_+e^{-i\varphi}\sin^2\frac{\theta}{2} + \widehat{L}_-e^{i\varphi}\cos^2\frac{\theta}{2}) + \frac{\lambda}{2}\widehat{S}_{-'}(-\widehat{L}_z\sin\theta + \widehat{L}_+e^{-i\varphi}\cos^2\frac{\theta}{2} - \widehat{L}_-e^{i\varphi}\sin^2\frac{\theta}{2})$, with an energy gain from matrix elements of the form $-\frac{\left|\langle i|\widehat{H}'_{SO}|j\rangle\right|^2}{\left|e_i-e_j\right|}$ where $i=|\mathbf{x}^2-\mathbf{y}^2\uparrow\rangle,|\mathbf{z}^2\uparrow\rangle$ and $j=|\mathbf{xy}\downarrow\rangle,|\mathbf{xz}\downarrow\rangle,|\mathbf{yz}\downarrow\rangle$ and e_i and e_j represent the corresponding orbital energies. These spin-orbit interactions occur between only occupied and unoccupied orbitals and those terms with small energy differences (i.e., $|e_i-e_j|$) significantly contribute to the SIA energy determining the spin direction. As can be seen

in Table 1, $|x^2 - y^2 \uparrow\rangle$ can interact with $|xy \downarrow\rangle$ through \hat{L}_z , leading to an *in-plane* SIA; $|x^2 - y^2 \uparrow\rangle/|z^2 \uparrow\rangle$ can interact with $|xz \downarrow\rangle$ through \hat{L}_+/\hat{L}_- , leading to SIA in the (010) plane; and $|x^2 - y^2 \uparrow\rangle/|z^2 \uparrow\rangle$ can interact with $|yz \downarrow\rangle$ through \hat{L}_+/\hat{L}_- , leading to the SIA in (100) plane.

The competitions among pairwise orbital interactions $|x^2 - y^2 \uparrow\rangle$ and $|xy \downarrow\rangle$, $|x^2 - y^2 \uparrow\rangle/|z^2 \uparrow\rangle$, and $|xz \downarrow\rangle/|yz \downarrow\rangle$ will be sensitive to any perturbations to the ligand-imposed crystal filed about the Fe site, because the nominal e_g symmetry orbitals $|x^2 - y^2 \uparrow\rangle, |z^2 \uparrow\rangle$ and the t_{2g} orbitals $|xy \downarrow\rangle$, $|xz \downarrow\rangle$, $|yz \downarrow\rangle$ are nearly degenerate, respectively. We then expect macroscopically different SIA directions due to the different displacive modes (see Figure 3). For this reason, SIA arising from such competitions can be tuned through a structural phase transition, manifesting as changes to the active modes that describe the equilibrium structures on either side of the transition. Even in the same structure, if the environments of the magnetic ions exhibit different symmtries, the SIA should be considerably different for those sites, such as those in the $P2_1/m$ phase. Therefore, we attribute the physical origins to the easily structure-tunable competitions among the interactions between the t_{2g} and e_g orbitals on the Fe³⁺ site through SOC effects. This effect leads to an *easy-plane* perpendicular to x, y, and z through $|x^2 - y^2 \uparrow\rangle/|z^2 \uparrow\rangle$ and $|yz \downarrow\rangle$, $|x^2 - y^2 \uparrow\rangle/|z^2 \uparrow\rangle$ and $|xz \downarrow\rangle$, and $|x^2 - y^2 \uparrow\rangle$ and $|xy \downarrow\rangle$ interactions, respectively.

2.5 Tunable magnetic anisotropy in AA'BB'O₆ double perovskites

Although we predict the ferroelectric control of the magnetic anisotropy in HIF (ABO₃)₁/(A'BO₃)₁ superlattices with BiFeO₃/LaFeO₃ as a representative compound, the magnetic state is usually

antiferromagnetic (G-type spin order in BiFeO₃/LaFeO₃), despite weak ferromagnetism arising from the DM interactions [i.e., the second term in eq. (1)]. Here, we are more interested in applying the above mechanism to ferromagnetic or ferrimagnetic materials, which is technologically preferable. We next examine the recently proposed HIF AA'BB'O₆ double perovskites [60], i.e., LaRNiMnO₆ (R is the rare-earth ion), in which both ferroelectricity in the polar-chiral P2₁ structure and strong ferromagnetism (1.54 μ_B for Ni²⁺ and 3.13 μ_B for Mn⁴⁺ [60]) were predicted but without apparent strong magnetoelectric coupling. We first confirm that the P-to-NP transition occurs in HIF AA'BB'O₆ double perovskites, using LaYNiMnO₆ as an experimentally accessible member of the LaRNiMnO₆ (R is the rare-earth ion) family by considering that the Bi₂NiMnO₆/La₂NiMnO₆ superlattices were experimentally synthesized [61]. Figure 1c shows that the polar-to-nonpolar ($P2_1$ -to- $P\overline{1}$) transition occurs at $\approx 0\%$ strain along with a sudden change of the polarization from 9 µC/cm² to zero. We next investigate whether the structure- and orbitalbased magnetocrystalline anisotropy theory previously described for HIF (ABO₃)₁/(A'BO₃)₁ superlattices also applies to HIF AA'BB'O₆ double perovskites.

Our DFT+U+SOC calculations on LaYNiMnO₆ show that the magnetic anisotropy in polar $P2_1$ with FM spin order is along the *out-of-plane* direction, whereas it switches to be mostly in the $(1\bar{1}0)$ plane with a 50% decrease in the *out-of-plane* component in $P\bar{1}$. The SIA model also reveals a large difference in the magnetic anisotropy between the two phases as displayed in Figure 1d, although the magnetic anisotropy slightly deviates away from the *out-of-plane* direction predicted by SIA model in $P2_1$ compared with our direct DFT calculations. Our symmetry-mode analysis of

the SIA shows [53], as in the ferrate superlattice, that the *in-phase* and *out-of-phase* OOR modes exert the same effect on the SIA. In addition, the OOT mode dominates the OOR contribution in determining the SIA direction. The magnetic anisotropy in the nonpolar $P\bar{1}$ phase is ultimately determined by further including the AFE modes induced by the OOT modes. Therefore, the decoupling of the OOT modes also results in the different SIA on the magnetic ions, thus leading to very different magnetic anisotropies between the two AA'BB'O6 double perovskites phases.

Next, we assess whether it is the same physical orbital interactions as in the HIF (ABO₃)₁/(A'BO₃)₁ superlattices that permit the change of the magnetic anisotropy across the P-to-NP transition. First, we identify the orbital configurations of Mn⁴⁺ and Ni²⁺ in LaYNiMnO₆ from Figure 4b and 4c (see also Ref. [53]). In the polar $P2_1$ phase, we find $(|xy\uparrow\rangle, |xz\uparrow\rangle, |yz\uparrow\rangle)^1 < (|x^2-y^2\uparrow\rangle, |z^2\uparrow\rangle$))⁰<($|xy\downarrow\rangle$, $|xz\downarrow\rangle$, $|yz\downarrow\rangle$)⁰<($|x^2-y^2\downarrow\rangle$, $|z^2\downarrow\rangle$)⁰ and in the nonpolar $P\overline{1}$ structure we find ($|xy\uparrow\rangle$ $(|xz\uparrow\rangle, |yz\uparrow\rangle)^1 < (|x^2-y^2\uparrow\rangle, |z^2\uparrow\rangle)^1 < (|xy\downarrow\rangle, |xz\downarrow\rangle, |yz\downarrow\rangle)^1 < (|x^2-y^2\downarrow\rangle, |z^2\downarrow\rangle)^0$ for Mn⁴⁺ and Ni²⁺ ions, respectively. It should be noted that neither the xy, xz, yz orbitals in either the spinup or spin-down manifolds are degenerate nor are the $|x^2-y^2\rangle,|z^2\rangle$ orbitals. From perturbation theory, we find that the SOC interactions will mix $(|xy\uparrow\rangle, |xz\uparrow\rangle, |yz\uparrow\rangle)^1$ and $(|x^2-y^2\uparrow\rangle, |z^2\uparrow\rangle$ $\rangle)^0$ on Mn^{4+} and $(|xy\downarrow\rangle, |xz\downarrow\rangle, |yz\downarrow\rangle)^1$ and $(|x^2-y^2\downarrow\rangle, |z^2\downarrow\rangle)^0$ on Ni^{2+} through the spinconserving terms: $\hat{H}_{SO}^0 = \lambda \hat{S}_{z'} \left(\hat{L}_z \cos\theta + \frac{1}{2} \hat{L}_+ e^{-i\varphi} \sin\theta + \frac{1}{2} \hat{L}_- e^{i\varphi} \sin\theta \right)$. As can be seen in Table 1, for Mn^{4+} , $|x^2-y^2\uparrow\rangle$ can interact with $|xy\uparrow\rangle$ through \hat{L}_z , leading to *out-of-plane* SIA; $|x^2 - y^2 \uparrow\rangle/|z^2 \uparrow\rangle$ can interact with $|xz \uparrow\rangle$ through \hat{L}_+/\hat{L}_- , leading to *in-plane* SIA along the ydirection; and $|x^2 - y^2 \uparrow\rangle/|z^2 \uparrow\rangle$ can interact with $|yz \uparrow\rangle$ through \hat{L}_+/\hat{L}_- , leading to *in-plane*

SIA along the x direction. Because the energy levels of the $|x^2 - y^2| \uparrow \rangle$, $|z^2| \uparrow \rangle$ states and $|xy| \uparrow$), $|xz\uparrow\rangle$, $|yz\uparrow\rangle$ are nearly degenerate, the competitions among the interactions between $|x^2$ $y^2 \uparrow$ and $|xy \uparrow\rangle$ and between $|x^2-y^2 \uparrow\rangle/|z^2 \uparrow\rangle$ and $|xz \uparrow\rangle/|yz \uparrow\rangle$ are highly susceptible to changes in the coordination geometry of the magnetic ions, which enables structure-based control over the orbital interactions and SIA. We deduce similar conclusions for Ni²⁺ between (|xy| $(|x^2 - y^2|)^1$ and $(|x^2 - y^2|)^1$. Therefore, the structural-tunable competitions among the interactions between the t_{2g} and e_g orbitals on the magnetic ions through SOC effects is also the origin of the ferroelectric control of the magnetic anisotropy in HIF AA'BB'O6 double perovskites. The most striking phenomenon here is the ferroelectric control of strong out-of-plane ferromagnetism in LaYNiMnO₆ through the P-to-NP transition. Even with antiferromagnetic spin order in AA'BB'O6 double perovskites, the ferroelectric control of large out-of-plane magnetization (i.e., ferrimagnetism) may also be realized by chemical selection of magnetic moments of the B and B' cations, such as in Ca₂FeOsO₆ and Ca₂FeMoO₆ compounds with G-type spin orders in the $P2_1/n$ structure [62,63]. This centrosymmetric $P2_1/n$ structure is a potential candidate for realizing the P2₁ polar structure in the AA'BB'O₆ chemistry if A-site substitution can achieve [001] layered cation order, for example, in a thin film along the crystal-growth direction [64,65].

We finally compute the energy barriers corresponding to viable transition paths between $Pmc2_1$ and $P2_1/m$ in BiFeO₃/LaFeO₃ and between $P2_1$ and $P\overline{1}$ in LaYNiMnO₆ [66]. We find that the energy barrier in BiFeO₃/LaFeO₃ can be as low as 77 meV/f.u. [53], which is much smaller than

completely switching the polarization in $Pmc2_1$ to its opposite direction (136 meV/f.u.) [42]. There are two reasons for the low energy barrier for the $Pmc2_1$ to $P2_1/m$ transition: first, we consider a "two-step" transition process. The polar-to-nonpolar transition is part of the polarization reversal process, which is energetically more favorable than a one-step process through a higher energy intermediate [67,68]. Second, our nonpolar phase, which serves as the intermediate state for the polarization reversal [67,68], is also low in energy. The energy barrier is 242 meV/f.u in LaYNiMnO₆ [53]. A previous study indicated that the energy barrier can be reduced either by using compressive strain or by chemical substitution to achieve smaller OOR and OOT angles [42,69], which may be helpful for finding other compounds exhibiting ferroelectric control of strong *out-of-plane* ferromagnetism in LaRNiMnO₆ (R is the rare-earth ion) [60] near room temperature through the ferroelectric ($P2_1$)-to-antiferroelectric (P1) phase transition.

3. Discussion on the possible ferroelectric control of the perpendicular magnetic anisotropy Although there are many efforts at delivering ferroelectric control of the perpendicular magnetic anisotropy, these strategies are based on interfacial effects and leverage the strain generated by the substrate or changes of the electronic structures at the interfaces under an applied electric field [12-15,34,70]. Intrinsic ferroelectric control of the perpendicular magnetic anisotropy in multiferroics without strain mediation remains rare. Our study delivers microscopic insight into the application of recent magnetic anisotropy control by oxygen octahedral tilt in the field of ferroelectric control of the perpendicular magnetic anisotropy [71,72], where the *out-of-plane* magnetization can be changed in our studies, due to the changes of the magnetic anisotropy.

Moreover, ferroelectric control of the perpendicular magnetic anisotropy offers advantages over electric control of the transition between antiferromagnetic and ferromagnetic spin orders [27-29]. The former case relies on the change of SIA energy, which is much weaker than changing the spin-exchange interactions among the magnetic ions [see the first term in eq. (1)] in the latter case. The lower magnetic transition barrier may facilitate the simultaneous change of the electric and magnetic signals in an application. Although there are other routes to control the magnetic anisotropy, such as strain effects [73], ions substitution [74], film reorientation [75] and varying thickness of the film with the changes of the oxygen octahedral tilt [71,72], they cannot be dynamically reversible.

Experimentally in thin films [12-15,34,73], consideration of shape anisotropy is another importance factor which usually leads to *in-plane* magnetic anisotropy in FM thin films, but disappears in bulk samples. The influence of this effect can be minimized or overcome by judicious choice of operating temperature or strain [76-78]. If the magnetic anisotropy is strong as in Fe, Os and Mo compounds [36,62,63,65], the effects of the shape anisotropy can be negligible. There are also magnetic domains and domain walls in thin films. Compared with the ferroelectric domain walls, there frequently exists common 180° and 90° magnetic domain walls, with which the magnetization will be sensitive. For example, the polarization can be significantly weakened in 180° domain-wall structures and changes direction in 90° domain-walls [18-26], which is also the cases for the magnetization in the magnetic domain walls. Although the magnetic anisotropy can be switched through the P-to-NP transition, the macroscopic magnetization may be null in

180° domain-walls structure. If the polar and magnetic domains can be coupled to each other, such as in the coupling between polar and antiferromagnetic domains in BiFeO₃ [22], then the 90° domain-walls structure can be expected to realize switchable magnetic anisotropy macroscopically.

We further consider the effects of the temperature on the changes of the magnetic anisotropy across the phase transition. As shown in Figures 5(a) and 5(b), the Néel temperature in BiFeO₃/LaFeO₃ is around 500 K and the Curie temperature in LaYNiMnO6 is around 116 K at 0% strain. In BiFeO₃/LaFeO₃ the magnetic anisotropy in the $Pmc2_1$ phase is in plane along the x direction approach 0 K, while the spins point away from the in-plane direction in the $P2_1/m$ phase, oriented about 45° and in the yz plane [Figure 5(c)]. These results are consistent with the results from the model analysis based on the coefficients obtained from our DFT calculations. These differences in the magnetic anisotropies between the polar and nonpolar phases remain discernible up to 150K, where we find that most of the spins still lie in plane in the polar phase and many spins in the nonpolar phase are oriented 45° away from the in-plane orientation and close to the yz plane. We also find that the width of the peak, indicating the out-of-plane spin direction (φ) , becomes broader at higher temperature, which indicates that thermal effects effectively reduce the magnetic anisotropy term in the spin Hamiltonian. As a result, the spin orientations are more broadly distributed.

In LaYNiMnO₆ upon approaching 0 K, the magnetic anisotropy in the $P2_1$ phase is close to the z axis (around 75°) and the yz plane. In contrast in the $P\overline{1}$ phase, the spins are oriented close to the

in-plane direction around 30° and lie close to the y axis (around -120°). These temperature-dependent anisotropies are consistent with the results from the model analysis coefficients obtained from our DFT calculations. This difference in the magnetic anisotropies between the polar and nonpolar phases remains discernible up to 40 K. We can also see that the position of magnetic anisotropy varies more widely at higher temperature in LaYNiMnO₆. For example, at 40 K the magnetic anisotropy in the polar phase approaches the in-plane direction and spins aligned along the in-plane spin direction tend towards the x direction, which is oppose to the behavior observed at lower temperatures. In contrast, the spin alignment in BiFeO₃/LaFeO₃ evolves smoothly with temperature. The reason for the stronger temperature-dependent loss in spin orientational preferences in LaYNiMnO₆ may be attributed to its weaker magnetic anisotropy compared to BiFeO₃/LaFeO₃.

Our study also provides an alternative route to find materials with large voltage control of magnetic anisotropy (VCMA) coefficient (Figure 6 and refs. [53,80-82]). The VCMA coefficient in the single-component multiferroics, resulting from the ferroic phase transition induced changes in the perpendicular magnetic anisotropy (i.e., the out-of-plane magnetization in our case), can be as large as $\sim 10^5$ in Bi₂MnReO₆. Thus, we show in theory that the VCMA coefficient in Bi₂MnReO₆ can be two orders larger than those found in magnetic tunnel junctions (MTJs), which indicates strong modulation of H_r (resonance field) and H_c (magnetic coercive field) under an applied electric field. Even in LaYNiMnO₆ with its weak magnetic anisotropy, we predict the VCMA coefficient can be comparable to the VCMA coefficients in MTJs (Figure 6).

4. Conclusions

Our theory is neither limited to the compounds presented in this work nor limited to HIF materials (see Table 2), because the basic approach for the magnetic anisotropy control are based on two principles: First, how the d orbitals split under an octahedral field: selecting magnetic ions in the compound having d orbital configurations with the highest-occupied or lowest-unoccupied orbitals including a xy orbital nearly degenerate with at least one of the other two t_{2g} orbitals. For example, this criterion is satisfied by choosing ions with d³, d⁵ or d⁸ electron fillings on at least one magnetic octahedral site in the crystal. Note that our theory does not apply to magnetic ions with orbital degeneracies such that the highest occupied orbital is degenerate with the lowest unoccupied orbital so as to yield a first-order Jahn-Teller instability [52,59]. The Jahn-Teller distortion would lift the degeneracy and result in a dominate SOC interaction between the highest occupied orbital degenerate with the lowest unoccupied orbital. In this case, the SIA is solely determined by this SOC interaction and there are no competing (comparable in energy) interactions available for modulation. Next, a polymorphism criterion: ferroelectric-ferroelectric or ferroelectricantiferroelectric phase competitions between two structures having significantly different magnetic ion coordination environments. Examples of transitions involving these changes in the BO₆ octahedral geometry include HIF with changes in the OOT pattern and competitive ferroic phases in thin films with different symmetries. The transitions between the two states involved in the polymorphism can be realized by carefully investigating potential metastable structures and assessing their different coupling to an electric field through a $P \cdot E$ term [83,84]. Our theory is

quite flexible in realization and may pave a way to find the ideal multiferroics for the application of so-called four-state memory devices [9].

Acknowledgements

X.-Z.L. and J.M.R. were supported by the National Science Foundation (NSF) through the Pennsylvania State University MRSEC under award number DMR-1420620. DFT calculations were performed on the CARBON cluster at the Center for Nanoscale Materials, the Extreme Science and Engineering Discovery Environment (XSEDE), which is supported by NSF (ACI-1548562), and the DoD Supercomputing Resource Centers supported by the High Performance Computing and Modernization Program of the DOD. Use of the Center for Nanoscale Materials, an Office of Science user facility, was supported by the U.S. Department of Energy, Office of Science, Office of Basic Energy Sciences, under Contract No. DE-AC02-06CH11357.

References

- [1] S. Manipatruni, D. E. Nikonov, C.-C. Lin, T. A. Gosavi, H. Liu, B. Prasad, Y.-L. Huang, E. Bonturim, R. Ramesh and I. A. Young, *Nature* **565**, 35–42 (2019).
- [2] S. Fusil, V. Garcia, A. Barthelemy and M. Bibes, Annu. Rev. Mater. Res. 44, 91 (2014).
- [3] D. Chiba, M. Yamanouchi, F. Matsukura and H. Ohno, Science 301, 943 (2003).
- [4] M. Weisheit, S. Fähler, A. Marty, Y. Souche, C. Poinsignon and D. Givord, *Science* **315**, 349 (2007).
- [5] D. Chiba, M. Sawicki, Y. Nishitani, Y. Nakatani, F. Matsukura and H. Ohno, *Nature* **455**, 515

(2008).

- [6] I. Stolichnov, S. W. E. Riester, H. J. Trodahl, N. Setter, A. W. Rushforth, K. W. Edmonds, R. P. Campion, C. T. Foxon, B. L. Gallagher and T. Jungwirth, *Nature Materials* 7, 464 (2008).
- [7] S.-W. Cheong and M. Mostovoy, *Nat. Mater.* **6**, 13 (2007).
- [8] R. Ramesh and N. A. Spaldin, *Nat. Mater.* **6**, 21 (2007).
- [9] M. Fiebig, T. Lottermoser, D. Meier and M. Trassin, *Nature Reviews Materials* 1, 16046 (2016).
- [10] C.-G. Duan, S. S. Jaswal and E. Y. Tsymbal, *Phys. Rev. Lett.* **97**, 047201 (2006).
- [11] J. M. Rondinelli, M. Stengel and N. A. Spaldin, *Nature Nanotechnology* **3**, 46 (2008).
- [12] T. Maruyama, Y. Shiota, T. Nozaki, K. Ohta, N. Toda, M. Mizuguchi, A. A. Tulapurkar, T. Shinjo, M. Shiraishi, S. Mizukami, Y. Ando and Y. Suzuki, *Nature Nanotechnology* **4**, 158 (2009).
- [13] W.-G. Wang, M. Li, S. Hageman and C. L. Chien, *Nat. Mater.* **11**, 64 (2012).
- [14] Y. Shiota, T. Nozaki, F. Bonell, S. Murakami, T. Shinjo and Y. Suzuki, *Nat. Mater.* 11, 39 (2012).
- [15] X. He, Y. Wang, N. Wu, A. N. Caruso, E. Vescovo, K. D. Belashchenko, P. A. Dowben and C. Binek, *Nat. Mater.* **9**, 579 (2010).
- [16] G. Radaelli, D. Petti, E. Plekhanov, I. Fina, P. Torelli, B. R. Salles, M. Cantoni, C. Rinaldi, D. Gutiérrez, G. Panaccione, M. Varela, S. Picozzi, J. Fontcuberta and R. Bertacco, *Nature Communications* 5, 3404 (2014).
- [17] J. A. Mundy, C. M. Brooks, M. E. Holtz, J. A. Moyer, H. Das, A. F. Rébola, J. T. Heron, J. D. Clarkson, S. M. Disseler, Z. Liu et al., Nature 537, 523-527 (2016).

- [18] J. Wang, J. B. Neaton, H. Zheng, V. Nagarajan, S. B. Ogale, B. Liu, D. Viehland, V. Vaithyanathan, D. G. Schlom, U. V. Waghmare, N. A. Spaldin, K. M. Rabe, M. Wuttig and R. Ramesh, *Science* 299, 1719 (2003).
- [19] T. Zhao, A. Scholl, F. Zavaliche, K. Lee, M. Barry, A. Doran, M. P. Cruz, Y. H. Chu, C. Ederer, N. A. Spaldin, R. R. Das, D. M. Kim, S. H. Baek, C. B. Eom and R. Ramesh, *Nat. Mater.* 5, 823 (2006).
- [20] Y.-H. Chu, L. W. Martin, M. B. Holcomb, M. Gajek, S.-J. Han, Q. He, N. Balke, C.-H. Yang, D. Lee, W. Hu, Q. Zhan, P.-L. Yang, A. Fraile-Rodriguez, A. Scholl, S. X. Wang and R. Ramesh, *Nat. Mater.* 7, 478 (2008).
- [21] T. Choi, Y. Horibe, H. T. Yi, Y. J. Choi, W. Wu and S.-W. Cheong, *Nature Mater.* **9**, 253–258 (2010).
- [22] J. T. Heron, M. Trassin, K. Ashraf, M. Gajek, Q. He, S. Y. Yang, D. E. Nikonov, Y.-H. Chu, S. Salahuddin and R. Ramesh, *Phys. Rev. Lett.* 107, 217202 (2011).
- [23] B. B. Van Aken, T. T.M. Palstra, A. Filippetti and N. A. Spaldin, *Nat. Mater.* **3**, 164-170 (2004).
- [24] Y. Kumagai and N. Spaldin, *Nature Commun.* **4**, 1540 (2013).
- [25] S. Artyukhin, K. T. Delaney, N. A. Spaldin and M. Mostovoy, *Nature Mater.* 13, 42–49 (2014).
- [26] H. Das, A. L. Wysocki, Y. Geng, W. Wu and C. J. Fennie, *Nature Communications* 5, 2998 (2014).
- [27] C. J. Fennie and K. M. Rabe, *Phys. Rev. Lett.* **97**, 267602 (2006).
- [28] J. H. Lee, L. Fang, E. Vlahos, X. Ke, Y. Woo Jung, L. F. Kourkoutis, J.-W. Kim, P. J. Ryan, T. Heeg, M. Roeckerath *et al.*, *Nature* **466**, 954-958 (2010).

- [29] J. H. Lee and K. M. Rabe, *Phys. Rev. Lett.* **104**, 207204 (2010).
- [30] E. Bousquet, M. Dawber, N. Stucki, C. Lichtensteiger, P. Hermet, S. Gariglio, J.-M. Triscone and P. Ghosez, *Nature* **452**, 732-736 (2008).
- [31] N. A. Benedek and C. J. Fennie, *Phys. Rev. Lett.* **106**, 107204 (2011).
- [32] A. B. Harris, *Phys. Rev. B* **84**, 064116 (2011).
- [33] J.M. Rondinelli and C. J. Fennie, *Adv. Mater.* **24**, 1961-1968 (2012).
- [34] S. Ikeda, K. Miura, H. Yamamoto, K. Mizunuma, H. D. Gan, M. Endo, S. Kanai, J. Hayakawa, F. Matsukura and H. Ohno, *Nature Mater.* **9**, 721 (2010).
- [35] A. Hirohata, W. Frost, M. Samiepour and J.-Y. Kim, *Materials* 11, 105 (2018).
- [36] P. S. Wang, W. Ren, L. Bellaiche and H. J. Xiang, *Phys. Rev. Lett.* **114**, 147204 (2015).
- [37] J. Feng, K. Xu, L. Bellaiche and H. J. Xiang, New J. Phys. 20 053025 (2018).
- [38] Y. S. Oh, X. Luo, F.-T. Huang, Y. Wang and S.-W. Cheong, *Nature Mater.* 14, 407-413 (2015).
- [39] M. S. Senn, A. Bombardi, C. A. Murray, C. Vecchini, A. Scherillo, X. Luo and S. W. Cheong, Phys. Rev. Lett. 114, 035701 (2015).
- [40] X. Q. Liu, J. W. Wu, X. X. Shi, H. J. Zhao, H. Y. Zhou, R. H. Qiu, W. Q. Zhang and X. M. Chen, Appl. Phys. Lett. 106, 202903 (2015).
- [41] M. H. Lee, C.-P. Chang, F.-T. Huang, G. Y. Guo, B. Gao, C. H. Chen, S.-W. Cheong and M.-W. Chu, *Phys. Rev. Lett.* 119, 157601 (2017).
- [42] Z. Zanolli, J. C. Wojdeł, J. Íñiguez and Ph. Ghosez, *Phys. Rev. B* **88**, 060102(R) (2013).
- [43] X.-Z. Lu and J. M. Rondinelli, *Nat. Mater.* **15**, 951 (2016).
- [44] X.-Z. Lu and J. M. Rondinelli, Adv. Funct. Mater. 27, 1604312 (2017).

- [45] J. P. Perdew, A. Ruzsinszky, G. I. Csonka, O. A. Vydrov, G. E. Scuseria, L. A. Constantin, X. Zhou and K. Burke, *Phys. Rev. Lett.* **100**, 136406 (2008).
- [46] G. Kresse and J. Furthmüller, *Phys. Rev. B* **54**, 11169-11186 (1996).
- [47] G. Kresse and J. Furthmüller, *Comput. Mater. Sci.* **6**, 15-50 (1996).
- [48] G. Kresse and D. Joubert, *Phys. Rev. B* **59**, 1758-1775 (1999).
- [49] X.-Z. Lu and J. M. Rondinelli, *Phys. Rev. Materials* **2**, 054409 (2018).
- [50] X. Z. Lu, X. G. Gong and H. J. Xiang, Comput. Mater. Sci. 91, 310 (2014).
- [51] H. J. Xiang, E. J. Kan, S.-H. Wei, M.-H. Whangbo and X. G. Gong, *Phys. Rev. B* **84**, 224429 (2011).
- [52] H. Xiang, C. Lee, H.-J. Koo, X. Gong and M.-H. Whangbo, *Dalton Trans.* 42, 823 (2013).
- [53] See Supplemental Material at [URL will be inserted by publisher] for computational methods, Reliability of the PBEsol functional, steps to compute the magnetic anisotropy for the unit cell, SIA coefficients for the polar and nonpolar structures in BiFeO₃/LaFeO₃ and LaYNiMnO₆ compounds, strain effects on the magnetic anisotropy, effects of the DM-exchange interaction on the magnetic anisotropy in $P2_1$ and $P\overline{1}$ phases, density of states (DOS) and U and SOC effects, phonon modes and effects of each mode on the SIA in $P2_1$ and $P\overline{1}$ phases of LaYNiMnO₆, energy barriers between the $Pmc2_1$ and $P2_1/m$ phases at 0% strain of BiFeO₃/LaFeO₃ and between the $P2_1$ and $P\overline{1}$ phases at 0% strain of LaYNiMnO₆, the theory applied to the R3 and $P2_1/n$ phases Bi₂MnReO₆, and the VCMA coefficients in LaYNiMnO₆ and Bi₂MnReO₆.
- [54] T. Moriya, *Phys. Rev.* **120**, 91 (1960).

- [55] T. Moriya, *Phys. Rev. Lett.* **4**, 228 (1960).
- [56] M. Matsuda, R. S. Fishman, T. Hong, C. H. Lee, T. Ushiyama, Y.Yanagisawa, Y. Tomioka and T. Ito, *Phys. Rev. Lett.* **109**, 067205 (2012).
- [57] C. Weingart, N. Spaldin and E. Bousquet, *Phys. Rev. B* **86**, 094413 (2012).
- [58] X. Ke, T. Birol, R. Misra, J.-H. Lee, B. J. Kirby, D. G. Schlom, C. J. Fennie and J. W. Freeland, Phys. Rev. B 88, 094434 (2013).
- [59] M.-H. Whangbo, E. E. Gordon, H. Xiang, H.-J. Koo and C. Lee, *Acc. Chem. Res.* **48**, 3080–3087 (2015).
- [60] H. J. Zhao, W. Ren, Y. Yang, J. Íñiguez, X. M. Chen and L. Bellaiche, *Nat. Commun.* 5, 4021 (2014).
- [61] P Padhan, P LeClair, A Gupta, M A Subramanian and G Srinivasan, *J. Phys.: Condens. Matter* **21** 306004 (2009).
- [62] C. Ritter, M. R. Ibarra, L. Morellon, J. Blasco, J. García and J. M. De Teresa, *J. Phys.: Condens. Matter* **12**, 8295–8308 (2000).
- [63] H. L. Feng, M. Arai, Y. Matsushita, Y. Tsujimoto, Y. Guo, C. I. Sathish, X. Wang, Y.-H. Yuan,M. Tanaka and K. Yamaura, J. Am. Chem. Soc. 136, 3326 (2014).
- [64] G. King and P. M. Woodward, *J. Mater. Chem.* **20**, 5785 (2010).
- [65] M. Ležaić and N. A. Spaldin, *Phys. Rev. B* **83**, 024410 (2011).
- [66] G. Henkelman, B. P. Uberuaga and H. A Jónsson, J. Chem. Phys. 113, 9901 (2000).
- [67] J. T. Heron, J. L. Bosse, Q. He, Y. Gao, M. Trassin, L. Ye, J. D. Clarkson, C. Wang, J. Liu, S. Salahuddin, D. C. Ralph, D. G. Schlom, J. Íñiguez, B. D. Huey and R. Ramesh, *Nature* **516**,

- 370-373 (2014).
- [68] E. A. Nowadnick and C. J. Fennie, *Physical Review B* **94**, 104105 (2016).
- [69] A. T. Mulder, N. A. Benedek, J. M. Rondinelli and C. J. Fennie, *Adv. Func. Mater.* **23**, 4810 (2013).
- [70] Q. Yang, T. Nan, Y. Zhang, Z. Zhou, B. Peng, W. Ren, Z.-G. Ye, N. X. Sun and M. Liu, *Phys. Rev. Applied* 8, 044006 (2017).
- [71] Z. Liao, M. Huijben, Z. Zhong, N. Gauquelin, S. Macke, R. J. Green, S. Van Aert, J. Verbeeck, G. Van Tendeloo, K. Held, G. A. Sawatzky, G. Koster and G. Rijnders, *Nat. Mater.* 15, 425 (2016).
- [72] D. Kan, R. Aso, R. Sato, M. Haruta, H. Kurata and Y. Shimakawa, *Nat. Mater.* 15, 432 (2016).
- [73] C. Du, R. Adur, H. Wang, A. J. Hauser, F. Yang and P. C. Hammel, *Phys. Rev. Lett.* **110**, 147204 (2013).
- [74] D. Yi, C. L. Flint, P. P. Balakrishnan, K. Mahalingam, B. Urwin, A. Vailionis, A. T. N'Diaye,P. Shafer, E. Arenholz, Y. Choi, et al., Phys. Rev. Lett. 119, 077201 (2017).
- [75] J. H. Lee, K. T. Delaney, E. Bousquet, N. A. Spaldin and K. M. Rabe, *Phys. Rev. B* 88, 174426 (2013).
- [76] G. Bayreuther, M. Dumm, B. Uhl, R. Meier and W. Kipferl, *Journal of Applied Physics* **93**, 8230 (2003).
- [77] M. Belmeguenai, S. Mercone, C. Adamo, L. Méchin, C. Fur, P. Monod, P. Moch and D. G. Schlom, *Phys. Rev. B* 81, 054410 (2010).
- [78] G. Shibata, M. Kitamura, M. Minohara, K. Yoshimatsu, T. Kadono, K. Ishigami, T. Harano, Y.

- Takahashi, S. Sakamoto, Y. Nonaka et al., npj Quantum Materials 3, 3 (2018).
- [79] K. Hukushima and K. Nemoto, J. Phys. Soc. Jpn. 65, 1604 (1996).
- [80] K. L. Wang, J. G. Alzate and P. Khalili Amiri, J. Phys. D: Appl. Phys. 46, 074003 (2013).
- [81] M. Liu and N. X. Sun, *Phil. Trans. R. Soc. A* **372**, 20120439 (2014).
- [82] P. V. Ong, N. Kioussis, D. Odkhuu, P. K. Amiri, K. L. Wang and G. P. Carman, *Phys. Rev. B* **92**, 020407(R) (2015).
- [83] K. M. Rabe, in *Functional Metal Oxides: New Science and Novel Applications*, edited by S. Ogale and V. Venkateshan (Wiley, New York, 2013).
- [84] J. W. Bennett, K. F. Garrity, K. M. Rabe and D. Vanderbilt, *Phys. Rev. Lett.* **110**, 017603 (2013).

Table 1. Values of (θ, φ) computed by minimizing $-|\langle i|\lambda \hat{L}\cdot \hat{S}|j\rangle|^2$, where $i, j=|xy\rangle$, $|xz\rangle$, $|yz\rangle$, $|x^2-y^2\rangle$ or $|z^2\rangle$. The definition of (θ, φ) is shown in the main text and '·' indicates the values are not available.

	xy>	xz>	yz⟩	$ x^2-y^2\rangle$	$ z^2\rangle$		
12 2 2	<u> </u>			-	l		
$\lambda \hat{L} \cdot \hat{S} = \hat{H}_{SO}^{0}$ for SOC between spins with same directions							
(xy		$(\frac{\pi}{2},0)$	$(\frac{\pi}{2}, \frac{\pi}{2})$	$(0,\cdot)$			
(xz	$(\frac{\pi}{2}, 0)$		(0,·)	$(\frac{\pi}{2}, \frac{\pi}{2})$	$(\frac{\pi}{2}, \frac{\pi}{2})$		
(yz	$(\frac{\pi}{2}, \frac{\pi}{2})$	$(0,\cdot)$		$(\frac{\pi}{2},0)$	$(\frac{\pi}{2},0)$		
$\langle x^2-y^2 $	(0,·)	$(\frac{\pi}{2}, \frac{\pi}{2})$	$(\frac{\pi}{2}, 0)$				
⟨ z²	•	$(\frac{\pi}{2}, \frac{\pi}{2})$	$(\frac{\pi}{2}, 0)$				
$\lambda \hat{\boldsymbol{L}} \cdot \hat{\boldsymbol{S}} = \widehat{H}_{SO}^{'}$ for SOC between spins with opposite directions							
(xy	•	$(\cdot,\frac{\pi}{2})$	(·,0)	$(\frac{\pi}{2},\cdot)$			
⟨xz	$(\cdot,\frac{\pi}{2})$		$(\frac{\pi}{2},\cdot)$	(·,0)	(·,0)		
(yz	(·,0)	$(\frac{\pi}{2},\cdot)$		$(\cdot,\frac{\pi}{2})$	$(\cdot,\frac{\pi}{2})$		
(x ² -y ²	$(\frac{\pi}{2},\cdot)$	(·,0)	$(\cdot,\frac{\pi}{2})$				
⟨ z²		(·,0)	$(\cdot,\frac{\pi}{2})$				

Table 2. Compounds identified fulfilling the proposed Orbital Configuration and Ferroic Transition criteria to achieve changes in magnetic anisotropy (MA).

Compounds	d orbital configuration	Magnetism	Ferroic transition	MA changes
BiFeO ₃ /LaFeO ₃	d^5	Weak FM	$Pmc2_1$ -to- $P2_1/m$	$[1\bar{1}0]$ to $[011]$
LaYNiMnO ₆	d^3 and d^8	FM	$P2_1$ -to- $P\overline{1}$	[001] to [-0.44,- 0.73,0.52]
Bi ₂ MnReO ₆	d^3 and d^8	Ferrimagnetism	R3-to-P2/n	[0.49,0.64,0.60] to [001]

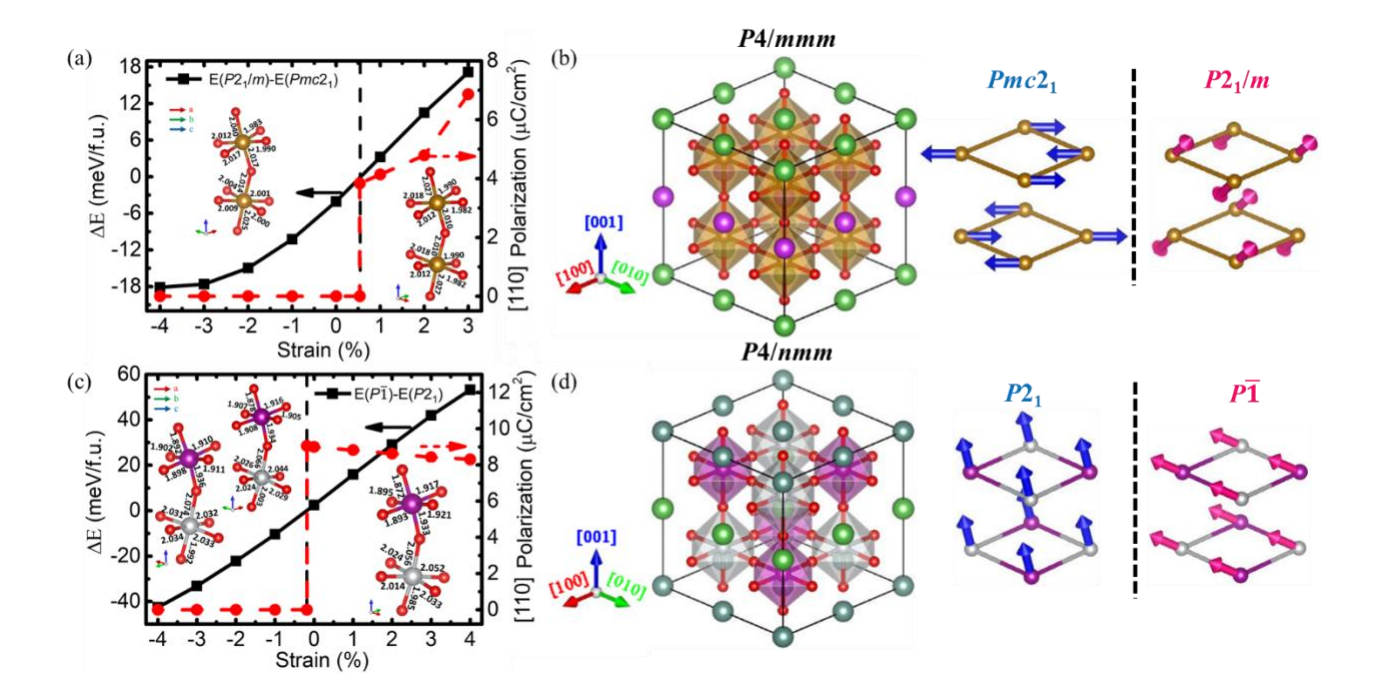


Figure 1. (a) Computed energies (left axis) and polarizations (right axis) with respect to the biaxial strain for BiFeO₃/LaFeO₃. The energy difference is between $P2_1/m$ and $Pmc2_1$. (b) The magnetic anisotropies in the $Pmc2_1$ and $P2_1/m$ phases. High-symmetry P4/mmm structure of BiFeO₃/LaFeO₃ is also shown on the left. The blue and pink arrows indicate the spins directions in $Pmc2_1$ and $P2_1/m$ phases, respectively. Only the iron sublattice is shown for clarity. (c) energies (left axis) and polarizations (right axis) with respect to the biaxial strain for LaYNiMnO₆. The energy difference is between $P\bar{1}$ and $P2_1$. (d) The magnetic anisotropies in the $P2_1$ and $P\bar{1}$ phases. High-symmetry P4/mmm structure of LaYNiMnO₆ is also shown on the left. The blue and pink arrows indicate the spins directions in $P2_1$ and $P\bar{1}$ phases, respectively. Only the manganese and nickel sublattice is shown. Insets in (a) and (c) show the comparison of the Fe-site coordination between $Pmc2_1$ (right) and $P2_1/m$ (left) phases and comparison of Mn- and Ni-site coordinations for the $P2_1$ (right) and $P\bar{1}$ (left) phases, respectively. Bond lengths are in unit of Å. The crystallographic axes are shown for the local environment.

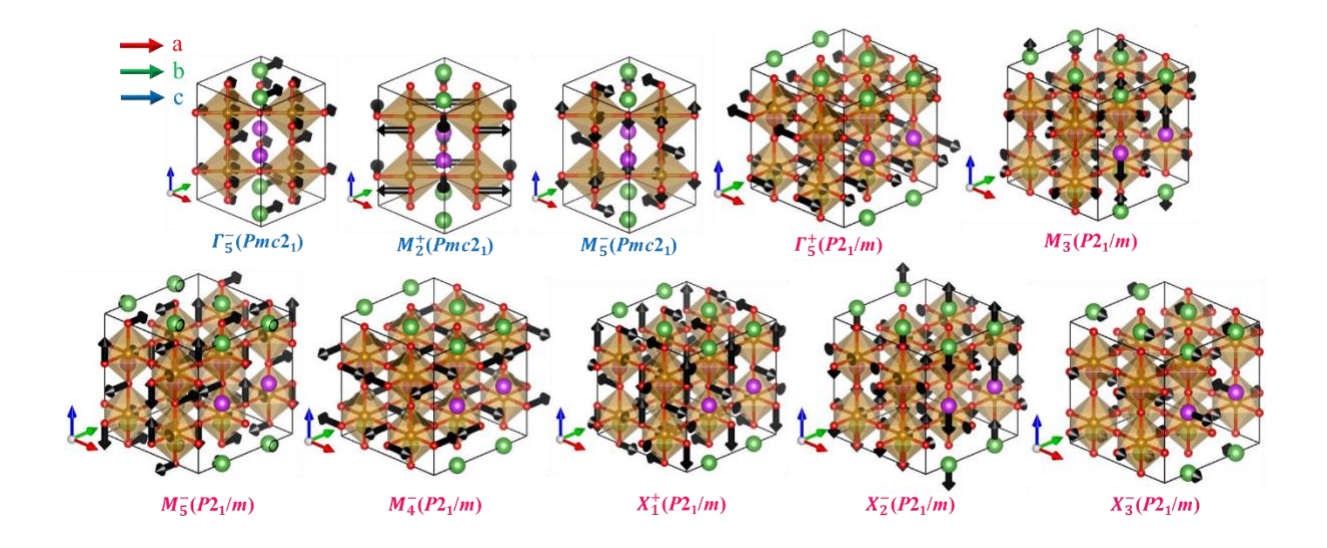


Figure 2. The modes in the $Pmc2_1$ and $P2_1/m$ structures are obtained by decomposing the ion displacements in each structure with respect to P4/mmm of BiFeO₃/LaFeO₃. Mode naming conventions follow that in Figure 2. The black arrows indicate the direction and magnitude of the ion displacements.

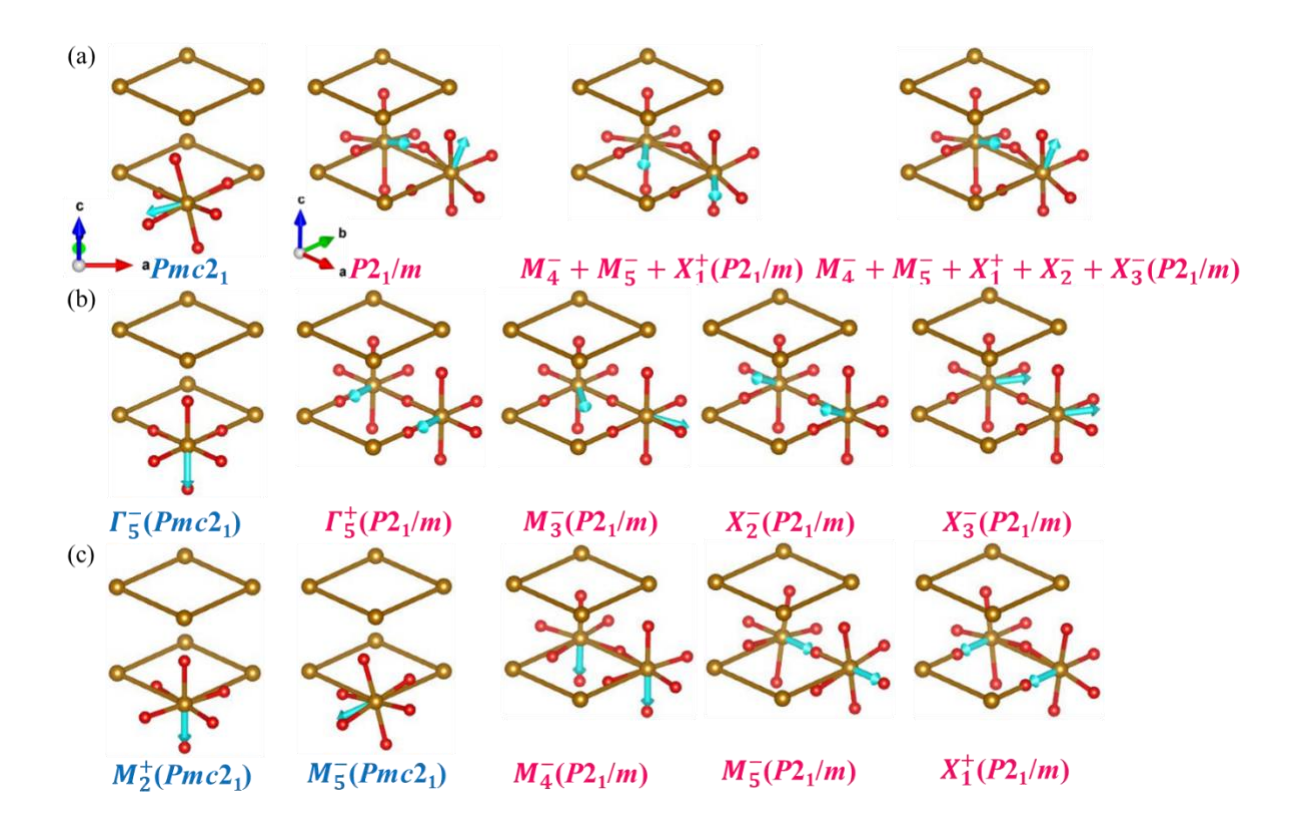


Figure 3. The single-ion anisotropy (SIA) obtained in BiFeO₃/LaFeO₃ with (a) multiple modes, (b) single (anti-)ferroelectric mode, and (c) single oxygen octahedral modes included in the P4/mmm structure. Each mode is represented by its irrep and corresponding symmetry. $Pmc2_1$ and $P2_1/m$ indicate that all the correlated modes leading to the specified symmetries are included. The light blue arrow indicates the direction of the single-ion anisotropy and only the iron sublattice and the local octahedron are shown for clarity. The crystallographic axes are shown for the two phases.

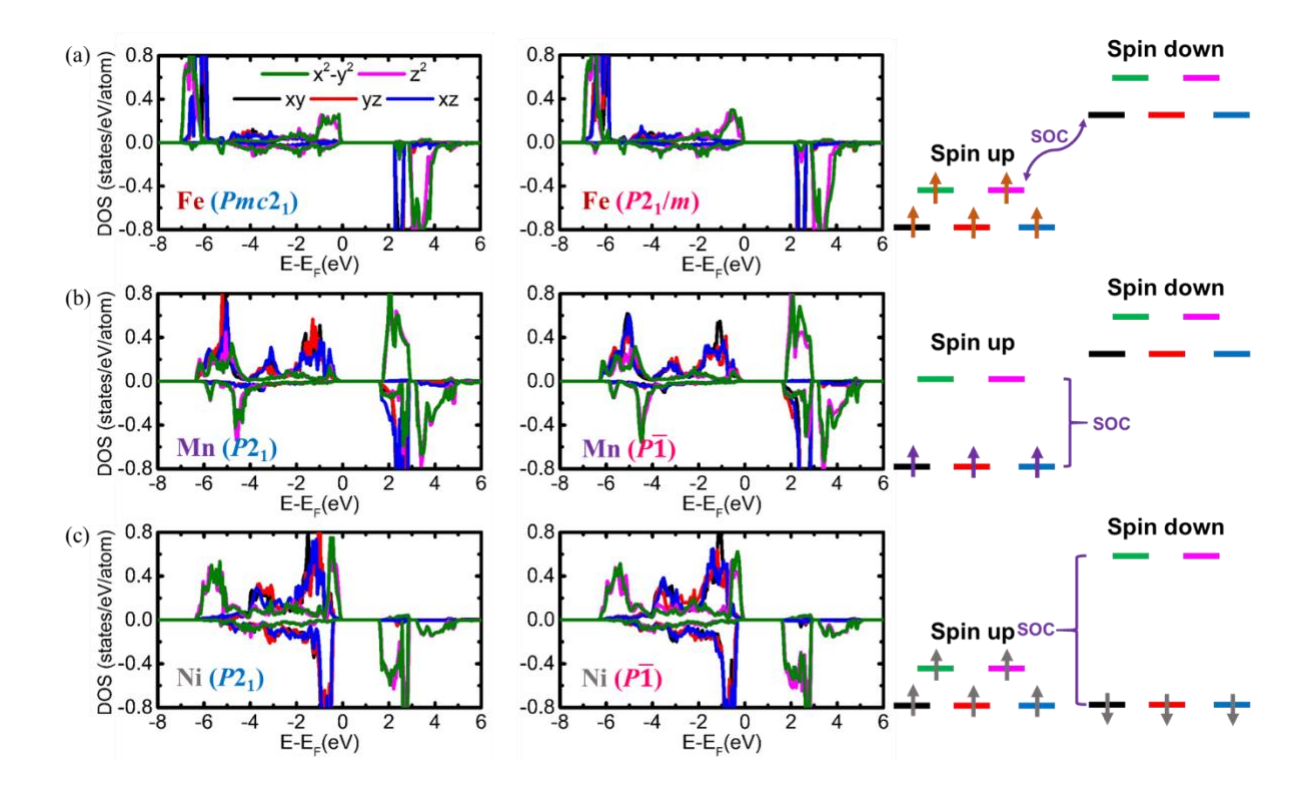


Figure 4. (a) Orbital project iron density of states (DOS) in $Pmc2_1$ and $P2_1/m$ and the schematic illustration of the orbital configuration in BiFeO₃/LaFeO₃. (b) and (c) show the density of states of manganese and nickel in $P2_1$ and $P\overline{1}$ and the schematic illustration of the corresponding orbital configurations in LaYNiMnO₆. There are two symmetry-inequivalent iron sites in $P2_1/m$ and two symmetry-inequivalent manganese and nickels, respectively, in $P\overline{1}$ and the density of states for the other iron in $P2_1/m$ and manganese and nickel in $P\overline{1}$ are shown in the SI. SOC is not included in these calculations.

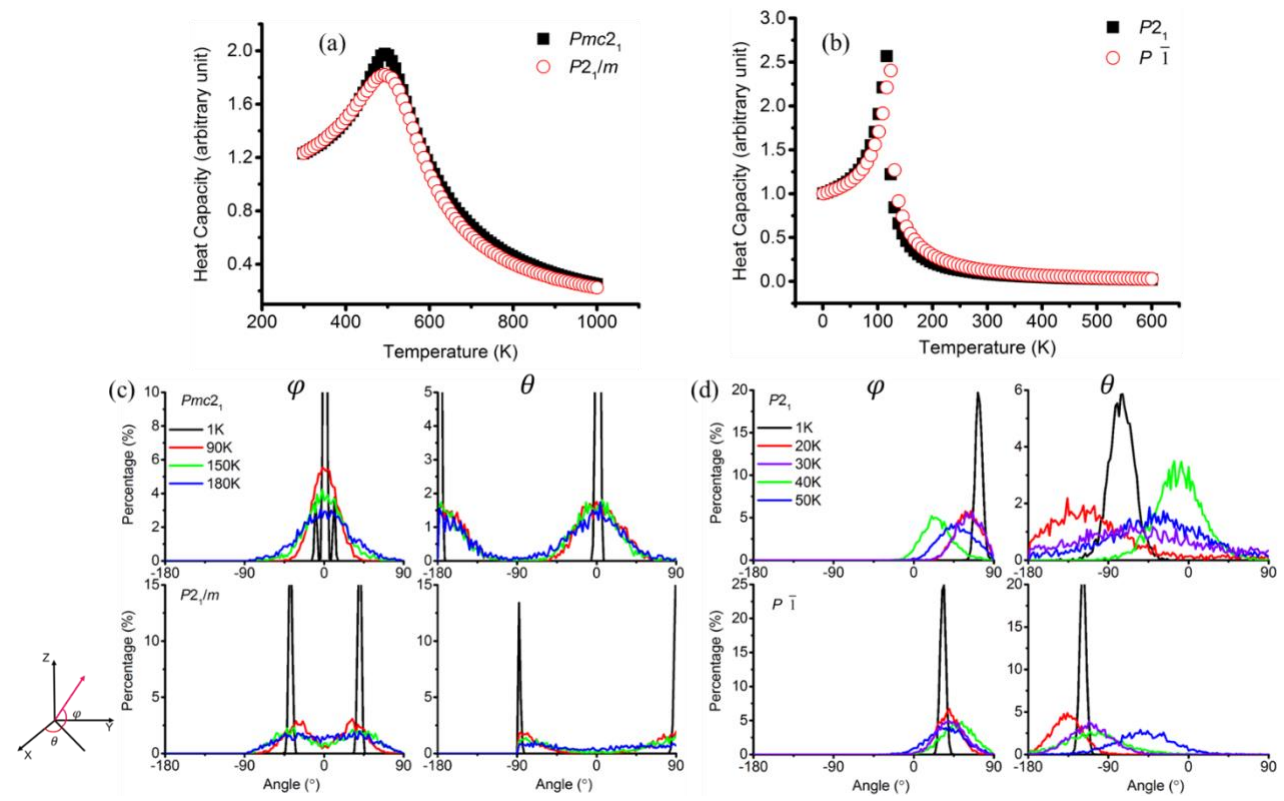


Figure 5. Magnetic transition temperatures for (a) BiFeO₃/LaFeO₃ and (b) LaYNiMnO₆ and temperature dependencies of the magnetic anisotropies in (c) BiFeO₃/LaFeO₃ and (d) LaYNiMnO₆, which are obtained by carrying out Monte Carlo simulations [53, 79]. Here, an $8 \times 12 \times 12$ supercell of the 20-atoms unit cell in $Pmc2_1$ and $P2_1$ phases was used and an $8 \times 8 \times 8$ supercell of the 40-atoms unit cell in $P2_1/m$ and $P\overline{1}$ phases was used in the Monte Carlo simulations. In the simulations, only symmetric spin exchange interactions in Eq. (1) were included for (a) and (b). In (c) and (d), we collected the spin directions in identically sized supercells, but both symmetric spin exchange interactions and single ion anisotropic terms in Eq. (1) were included. Percentage = (number of spin sites having the spin directions with the angles around θ and φ)/(number of all spin sites). Angles θ and φ are defined in the coordinate system as shown. They correspond to the in-plane angle about the x direction and the out-of-plane angle about the in-plane projection of the spin, respectively. It should be noted that there are two peaks in BiFeO₃/LaFeO₃, because its magnetic structure is antiferromagnetic and comprises two magnetic sublattices.

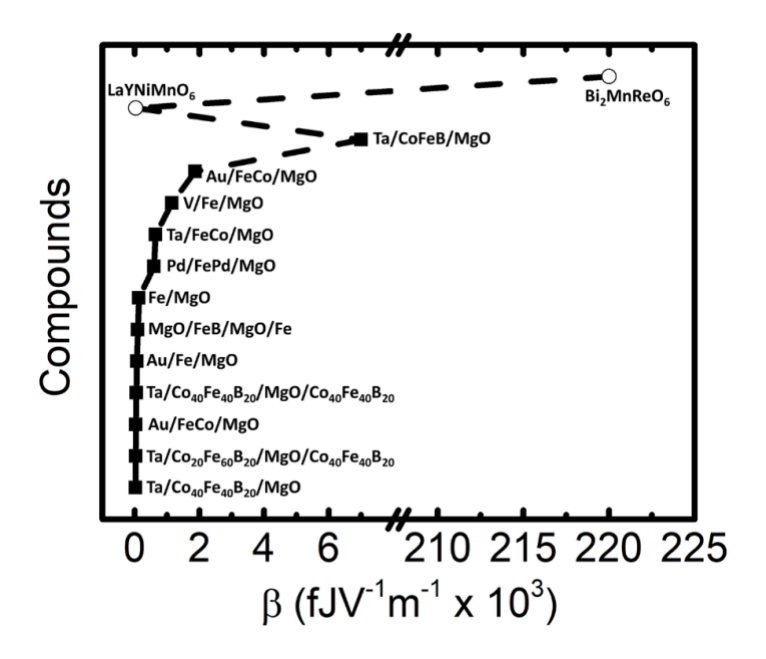


Figure 6. VCMA coefficient β in MTJ and multiferroic heterostructures. The opened circle represents the result from our work. $\beta = \frac{\Delta MA}{\Delta E_I}$ where ΔMA is the change of the perpendicular magnetic anisotropy (i.e., the changes of the out-of-plane magnetization in our study) induced by the change internal electric field ΔE_I . ΔE_I can be related to the external field (ΔE_{ext}) given the dielectric constant ε of the material: $\Delta E_I = \Delta E_{ext}/\varepsilon$. See [53] for references for reported β values.